Aluminate Red Phosphor in Light-Emitting Diodes: Theoretical calculations, Charge Varieties and High-pressure Luminescence Analysis

Niumiao Zhang[†, ‡], Yi-Ting Tsai[†], Mu-Huai Fang[†], Chong-Geng Ma[*, ⊥], Agata Lazarowska[§], Sebastian Mahlik[§], Marek Grinberg[§], Chang-Yang Chiang[#], Wuzong Zhou[#], Jauyn Grace Lin[$], Jyh-Fu Lee[&], Jiming Zheng[‡], Chongfeng Guo[*, ‡], Ru-Shi Liu[*, †, δ]

† Department of Chemistry, National Taiwan University, Taipei 106 (Taiwan)

‡ Institute of Photonics and Photon-Technology, Northwest University, Xi'an 710069 (China)

⊥ College of Sciences, Chongqing University of Posts and Telecommunications, Chongqing 400065 (China)

§ Institute of Experimental Physics, Faculty of Mathematics, Physics and Informatics, University of Gdansk, Wita Stwosza 57, 80-308 Gdansk (Poland)

EaStCHEM, School of Chemistry, University of St Andrews, St Andrews, KY169ST (United Kingdom)

$ Center for Condensed Matter Sciences, National Taiwan University, Taipei 106 (Taiwan)

& National Synchrotron Radiation Research Center, Hsinchu 300 (Taiwan)

δ Department of Mechanical Engineering and Graduate Institute of Manufacturing Technology, National Taipei University of Technology, Taipei 106 (Taiwan)

ABSTRACT: Searching for a non-rare earth-based oxide red-emitting phosphor is crucial for phosphor-converted light-emitting diodes (LEDs). In this study, we optimized a blue and UV-light excited $Sr_4Al_{14}O_{25}$:Mn phosphor exhibiting red emission peaked at ~653 nm, which was successfully synthesized by solid-state reaction. The crystal structure, micromorphology, and luminescent properties of $Sr_4Al_{14}O_{25}$:Mn phosphors were characterized by X-ray Rietveld refinement, high-resolution transmission electron microscopy, and photoluminescence spectra. The band gap and electronic structure of $Sr_4Al_{14}O_{25}$ were analyzed by density functional theory calculation using the hybrid exchange-correlation functional. The crystal field environment effect of Al sites from introducing activator Mn ions was investigated with the aid of Raman ^{27}Al nuclear magnetic resonance spectra and electron spin resonance. The pressure dependent on the luminescent properties and decay time of this compound were presented. The tri-color display spectrum by combining blue InGaN chips, commercial $\boldsymbol{\beta}$-SiAlON:Eu^{2+} green phosphor, and $Sr_4Al_{14}O_{25}$:Mn red phosphor were evaluated for commercial applications: using the present $Sr_4Al_{14}O_{25}$:Mn red phosphor converted LED as backlighting source.

■ INTRODUCTION

Since the emergence of energy shortage, relevant financial investments have been made to find new, persistent, clean energy sources or technologies for saving energy or developing new energy source. Comparing with the traditional incandescent and fluorescent lightings, white light-emitting diodes (LEDs) with good performance, long lifetime, high efficiency, and environmental benefits have attracted considerable attention. The key approach to generate commercial white LEDS (WLEDs) was combining a near ultraviolet (n-UV) chip with one or more phosphors, and most commercial WLEDs products were fabricated through coupling InGaN LED chip and yellow phosphor YAG:Ce^{3+}.[1–3] However, this design offers low colour rendering index (CRI, ≤ 80) and high correlated color temperature (CCT, ≥4500 K) caused by the deficient of red emission in YAG:Ce^{3+} phosphor.[4, 5] Now, nitride and sulfide based red phosphors are popular. The former, such as MAlSiN$_3$: Eu^{2+} [6] and M$_2$Si$_5$N$_8$: Eu^{2+} (M = Ca, Sr, Ba),[7] has been widely used in WLEDs because of their excellent performance in luminescent efficiency and thermal stability.[8–11] The latter sulfide -based red phos-

phors, such as $CaS:Eu^{2+}$ and $(Y, La)_2O_2S:Eu^{3+}$, are chemically unstable in humid environment.[12,13] Moreover, the reaction between the electrodes of a LED chip and sulfur can generate Ag_2S, thus limiting their applications. Thus, developing a novel red phosphor is necessary to improve the performance of the device. Compound $Sr_4Al_{14}O_{25}$ is one of the most promising candidates due to its convenient preparation through one step solid-state reaction at 1300 °C in air atmosphere. Recently, Peng et al.[14] have reported that the site occupancy preference of Mn^{4+} replace the Al^{3+} sites. Chen et al.[15] have researched the enhanced red luminescence by coupling $SrAl_2O_4$ phase with the $Sr_4Al_{14}O_{25}:Mn^{4+}$ system. But the electronic structure of host, crystal field environment effect of Al sites by introducing activator Mn ions, and the high-pressure luminescent properties of Mn-activated $Sr_4Al_{14}O_{25}$ have not been researched.[16, 17] Moreover, it can be also noted here that the applications of the external hydrostatic pressure allow us to straightforwardly manipulate the bonding lengths between the Mn^{4+} and nearest-neighbor O^{2-} ions and the related hybridization effect between the $Mn-3d(t_{2g})$ and $O-2p$ states, and thus further give a full play to tuning the Mn^{4+} red emission energy position,[18] which opens the feasibility to the optical performance optimization of such a red phosphor reported. In addition, it is desirable to quantitatively describe the correlation between the local structural and spectroscopic properties of Mn^{4+} ions in solids from the experimental point of view in order to get a mutual and consistent corroboration with those theoretical studies.[19, 20] The objectives of this study are to first figure out the electronic structure of the $Sr_4Al_{14}O_{25}$ host by calculation and investigate the crystal field environment effect in the process of substituting Al^{3+} by Mn^{4+}. The high-pressure luminescence properties of the phosphor were also characterized to obtain the Mn^{4+} red emission dependence on the pressure. The objectives were achieved through the hybrid density functional theory (DFT) calculation, in addition to multiple methods, such as Total Pattern Analysis Solutions (TOPAS) software, electron paramagnetic resonance (EPR), nuclear magnetic resonance (NMR), and high-pressure photoluminescence (PL). Finally, a phosphor-converted LED device as backlighting source was researched through exciting *β*-SiAlON:Eu^{2+} green and present red phosphor.

■ EXPERIMENTAL SECTION

Materials and sample preparation.

The samples of Mn-doped phosphors $Sr_4Al_{14}O_{25}$ were successfully synthesized from raw materials including analytical reagent $SrCO_3$, $Al(OH)_3$, $MnCO_3$, and MgO, and H_3BO_3 was adopted as flux. The raw materials were thoroughly grounded in a mortar. The mixing reactants were placed into the alumina boat crucible and heated with the rate of 5 °C min^{-1}; and then calcined at 1300 °C for 5 h in air. After calcining and cooling down to room temperature, the samples were transferred and obtained for further test.

Characterization.

The structure patterns and information of the samples were obtained by synchrotron X-ray diffraction analysis (λ = 0.774907 Å) using the BL01C2 beamline at the National Synchrotron Radiation Research Center (NSRRC), Taiwan. TOPAS software was used to the structural analysis by the X-ray Rietveld refinement. The high-resolution transmission electron microscopic (HRTEM) images were recorded on a Jeol JEM-2011 electron microscope operated at 200 kV at the University of St Andrews (St Andrews, KY16 9ST, United Kingdom). The photoluminescence (PL) and photoluminescence excitation (PLE) spectra were obtained on a FluoroMax-3 spectrophotometer (HORIBA, Japan) equipped with a 150 W Xe lamp and Hamamatsu R928 photomultiplier tube as the excitation source. Raman ^{27}Al MAS nuclear magnetic resonance (NMR) spectra were acquired on a wide-bore 14.1-Tesla Bruker Avance III NMR spectrometer, equipped with a 3.2 mm double-resonance magic-angle-spinning probe head. The Larmor frequency for ^{27}Al was 156.40 MHz. The samples were spun at 20 kHz. A selective $\pi/6$ pulse of 0.5 μs was used for central transition excitation. The recycle delay was 1 s. The chemical shift was referenced to 1 M $Al(NO_3)_3$ aqueous solution. The room temperature ESR measurement was carried out using a Bruker EMX spectrometer with the microwave frequency fixed at 9.8 GHz. The emission signal was analyzed by a Hamamatsu streak camera model C4334-01 and a Bruker Optics 2501S spectrograph. The luminescence decay timescale is allowed from 1 ns to 10 ms for this apparatus. High hydrostatic pressure was used in a Merrill Bassett-type diamond anvil cell (DAC). Polydimethylsiloxane oil was used as the pressure-transmitting medium, and pressure was measured by the shift of the R_1 luminescence line of ruby ($Al_2O_3:Cr^{3+}$).

Computational details.

The DFT calculations for $Sr_4Al_{14}O_{25}$ host were performed in the closed-shell form by using the periodic *ab* initio CRYSTAL14 code based on the linear combination of atomic orbitals method.[21] The hybrid exchange-correlation functional WC1PBE consisting of a PBE correlation part and a Wu-Cohen exchange part with a fractional mixing (16%) of the nonlocal Hartree-Fock exchange was employed in order to yield better agreement between the calculated and experimental electronic properties in this work.[22] The all-electron local Gaussian-type basis sets (BS's) in the form of 86-21d1G and 8-411d1G were used for Al and O atoms,[23, 24] respectively. For Sr atom, the scalar-relativistic small-core pseudo-potential of the Stuttgart/Cologne group was adopted,[25] and the corresponding valence BS was modified to provide a much better description to the host's electronic properties as follows: the primitive functions with exponents less than 0.1 Bohr^{-2} was removed and in addition one diffuse s and p function with exponent 0.12 were added, so that a [3s3p2d] form was obtained. The Monkhorst–Pack scheme for 8×8×8 *k*-point mesh in the Brillouin zone was applied. The truncation criteria for bielectronic integrals (Coulomb and HF exchange series) were correspondingly set to 8, 8, 8, 8, and 16. A default DFT integration grid was adopted together with much higher DFT density and grid

weight tolerances (values 8 and 16). The tolerance of the energy convergence on the self-consistent field iterations was set to 10^{-8} Hartree, and the convergence speed was facilitated by mixing 40% of the Hamiltonian matrix in the last cycle into the current cycle. In the geometry optimization calculation, the convergence criteria on the root-mean-square of the gradient and the nuclear displacement were set to 0.00006 Hartree/Bohr and 0.00012 Bohr, respectively. The calculated crystal structural parameters were given in Table S1 (as shown in Supporting Information) and there is a good agreement between them and the data in Table 1 obtained by the XRD Rietveld refinement. The electronic band structures and density of state (DOS) diagrams were calculated based on the fully optimized geometry structures.

■ RESULTS AND DISCUSSION

Figure 1a presents the XRD patterns of $Sr_4Al_{14}O_{25}$:Mn and the corresponding Rietveld refinement carried out by TOPAS software with R_{wp} = 10.73%, R_p = 7.14%, GOF =2.06, indicating that the phase of the sample is pure. The compound $Sr_4Al_{14}O_{25}$ exhibits an orthorhombic structure belonging to the Pmma space group, possessing the host lattice parameters of a = 24.7803(8) Å, b = 8.4797(3) Å, c = 4.8873(2) Å, which are identical with those in previous reports.[26, 27] The obtained unit cell volume of $Sr_4Al_{14}O_{25}$:Mn is 1026.9659 $Å^3$, which is larger than that of $Sr_4Al_{14}O_{25}$ (1025.7 $Å^3$). The reason is probably caused by the substitution of Al^{3+} with smaller ionic radii (R = 5.30 Å) in octahedral structure by larger Mn^{4+} (R = 5.35 Å).[28] **Figure 1b** displays the unit cell crystal structure of $Sr_4Al_{14}O_{25}$; the coordinates of atoms in the unit cell were listed in **Table 1**. As shown, the structure of $Sr_4Al_{14}O_{25}$ consists of six different crystallographic Al^{3+} sites: three AlO_4 tetrahedral (Al1, Al2, Al3) and three AlO_6 octahedral (Al4, Al5, Al6) sites. The AlO_4 tetrahedron are connected through sharing the corner atom (2×2 are the Al2 sites, or 3×3 are the Al1 and Al3 sites), which is similar to the structures of tri-coordinated oxygen atoms and tetrahedral triclusters in $SrAl_4O_7$[29] and mullite.[30] The AlO_6 octahedral chains connect each other by sharing one edge and are separated by the double-layer AlO_4 tetrahedral chains,[26, 27] which will be discussed later.
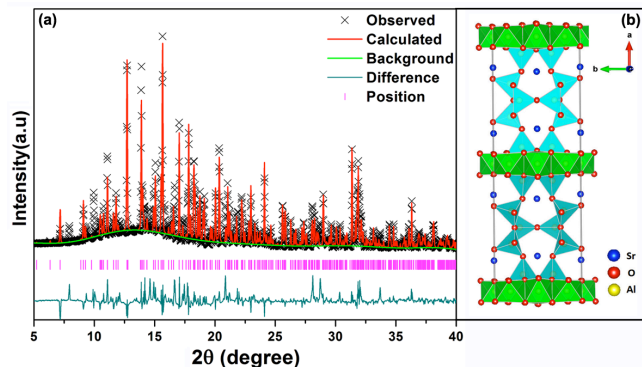
Figure 1. (a) XRD patterns of the Rietveld refinement of $Sr_4Al_{14}O_{25}$:Mn sample. (b) Unit cell crystal structure of $Sr_4Al_{14}O_{25}$.

To further investigate the $Sr_4Al_{14}O_{25}$:Mn crystals, transmission electron microscopy was performed to reveal microstructural information of the crystals. Many small fragments were observed from the crushed powder sample deposited on a copper grid with holey carbon film (**Figure 2a**). These fragments are the broken pieces from the original particles. The selected area electron diffraction patterns indicate that each fragment can be regarded as a single crystal, and can be indexed to the $Sr_4Al_{14}O_{25}$ phase, as shown in **Figure 2b**. The EDS result recorded from these fragments further confirms that the elemental ratio is rather similar to $Sr_4Al_{14}O_{25}$ (**Figure S1** and **Table S2**).
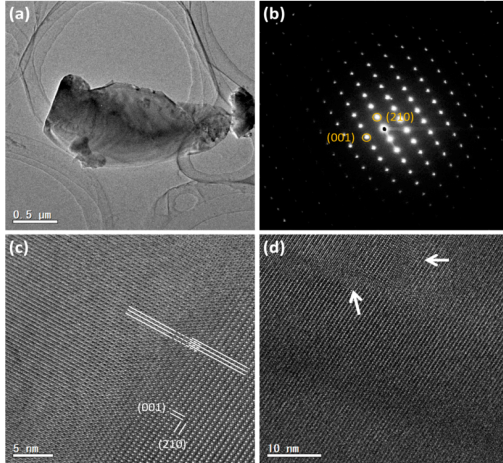
Domain structures were observed from the HRTEM images of most particles. **Figure 2c** is an image with anti-phase defects, whereas **Figure 2d** is an image showing a grain boundary of two domains. Although the crystallographic orientations of the two domains are the same, the (001) fringes shift about half unit cell across the boundary. This type of shift, giving an impression of anti-phase defects, can also be observed in between the domains in **Figure 2d**. However, the grain boundaries are not sharp enough to make an unambiguous conclusion of anti-phase defects. These defects may also be caused by distortion of crystal structure when manganese cations replace aluminum cations in tetrahedral or octahedral sites. Given that the manganese cations have different valence states (Mn^{4+} and Mn^{2+}) corresponding to different sites, change of the charge order in different areas may form these domains. **Figure S2** is another HRTEM image from a fragment, in which an obvious dark contract line appears. Although no break of lattice fringes is seen in this area, the dark contract can be an evidence of a defective area (or grain boundary). In our previous work,[31] by changing the view direction, a dark contrasted line in a "perfect" crystalline particle could actually be a boundary of twin plane. This kind of defect sometimes cannot be observed directly if the viewing direction is not parallel to the defect plane. Although the particles in the sample $Sr_4Al_{14}O_{25}$:Mn seem to be single crystals, some defects can be commonly observed.

Table 1. Structure parameter of red phosphors $Sr_4Al_{14}O_{25}$:Mn obtained by Rietveld refinement of the XRD data.*

Atom	symmetry	Wyckoff	x	y	z	Occu.	U(Å²)
Sr1	4	j	0.1376(1)	0.0005(1)	0.030(1)	1.0	0.0035
Sr2	4	i	0.1208(1)	0.0000(0)	0.1130(1)	1.0	0.0022
Al 1	8	l	0.1850(3)	0.1980(1)	0.6330(1)	1.0	0.0014
Al 2	8	l	0.0664(3)	0.3260(1)	0.5100(2)	1.0	0.0018
Al 3	4	k	0.2500(0)	0.2990(1)	0.1270(1)	1.0	0.0027
Al 4	4	g	0.0000(0)	0.1760(1)	0.0000(0)	1.0	0.0020
Al 5	2	c	0.0000(0)	0.0000(0)	0.0005(0)	1.0	0.0006
Al 6	2	b	0.0000(0)	0.5000(0)	0.0000(0)	1.0	0.0004

O1	8	l	0.0422(6)	0.1570(2)	0.3280(4)	1.0	0.0008
O2	8	l	0.1368(6)	0.3290(2)	0.5020(4)	1.0	0.0032
O3	8	l	0.1908(6)	0.2290(2)	0.0180(3)	1.0	0.0003
O4	4	k	0.2500(0)	0.2360(3)	0.4730(5)	1.0	0.0018
O5	4	i	0.0391(9)	0.0000(0)	0.8230(5)	1.0	0.0008
O6	4	j	0.0507(9)	0.5000(0)	0.3230(5)	1.0	0.0022
O7	4	i	0.1651(9)	0.0000(0)	0.5740(5)	1.0	0.0108
O8	8	l	0.0444(6)	0.3440(2)	0.8420(4)	1.0	0.0006
O9	2	f	0.2500(0)	0.5000(0)	0.0970(8)	1.0	0.0032

* **Space group: Pmma (51), $\alpha = \beta = \gamma = 90°$, a = 24.7703(84) Å, b = 8.4797(31) Å, c = 4.8833(17) Å, Z = 2, V = 1025.7193(62) Å^3, R_{wp} = 10.73 %, R_p = 7.14%, GOF = 2.06.**

Figure 3. PLE (λ_{em} = 653 nm) (blue line) and PL (λ_{ex} = 325 nm) (red line) spectra of $Sr_4Al_{14}O_{25}$:Mn^{4+} sample.

In order to provide the knowledge of the electronic structure of $Sr_4Al_{14}O_{25}$ with the reasonable estimation level, the calculated energy band structure of $Sr_4Al_{14}O_{25}$ host was obtained by using the hybrid HF-DFT method. **Figure 4** reveals that the top of valence band maximum (VBM) is located at the Y point of Brillouin zone, and the bottom of the conduction band minimum (CBM) is located at the G point, indicating that the host $Sr_4Al_{14}O_{25}$ is an indirect band-gap compound with a band gap of approximately 6.11 eV. The predicted host's band gap is very close to the experimental value of 6.5 eV for $SrAl_2O_4$ host,[40] and thus can be expected to be reliable if compared with experiment. As a reference, the DFT calculation with the generalized gradient approximation (GGA) form was also implemented and the band gap underestimation can be seen as shown by the calculated band gap value with 4.48 eV. It can be noted that those highest states of the valence band are nearly flat, whereas the conduction band is very dispersive, which means the electron mobility is higher than hole's in the compound. Such a phenomena is not unusual and has been reported in $SrAl_2O_4$.[41, 42]
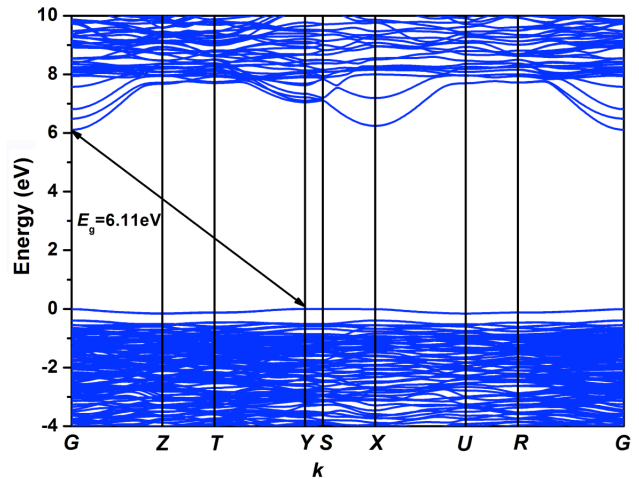

Figure 2. (a) A $Sr_4Al_{14}O_{25}$:Mn fragment; (b) SAED pattern recorded from the fragment; (c) HRTEM image with anti-phase domain (indicated by the marked parallel lines shifting in adjacent domain); (d) HRTEM image with some domain structures (pointed out by white arrows).

Figure 3 demonstrates the characteristic PLE and PL spectra of $Sr_4Al_{14}O_{25}$:Mn^{4+}. The PLE spectra monitored at 653 nm include a few broad absorption bands in the blue and ultraviolet (UV) region ranging from 260 to 500 nm. The lower energy band centered at 442 nm is attributed to the $^4A_{2g} \rightarrow {}^4T_{2g}$ transition of Mn^{4+}, and the higher energy band peaked at 352 nm is attributed to the $^4A_{2g} \rightarrow {}^4T_{2g}$ transition.[14] The band structure with the maximum at 325 nm can be related to the O^{2-}-Mn^{4+} charge transfer transition,[32-35] as the host absorption band is confirmed to be far away from the range by our first-principles calculations. By contrast, the PL spectra consist of double peaks at 653 and 666 nm from the $^2E_g \rightarrow {}^4A_{2g}$ transitions. First band at 653 nm is zero phonon line (ZPL) called R-line. In fact, it is the superposition of a number of ZPL lines (from different sites and low symmetry splitting the ^2E_g and $^4A_{2g}$ levels) which we observe as one broadened line.[36] Additionally, their phonon repetition sideband is observed at 666 nm, which is based on the Tanabe-Sugano diagram of the $3d^3$ electron configuration in the $[MnO^{6-}]^{8-}$ octahedral complex.[37–39] Results suggest that $Sr_4Al_{14}O_{25}$:Mn^{4+} is a promising red phosphor for LED with excitation of blue and ultraviolet (UV) chips.

Figure 4. Calculated energy band structure of $Sr_4Al_{14}O_{25}$. The letters *Γ, Z, T, Y, S, X, U,* and *R* represent the chosen high-symmetry *k* points: (0, 0, 0), (0, 0, 1/2), (0, 1/2, 1/2),

(0, 1/2, 0), (1/2, 1/2, 0), (1/2, 0, 0), (1/2, 0, 1/2), and (1/2, 1/2, 1/2), respectively.
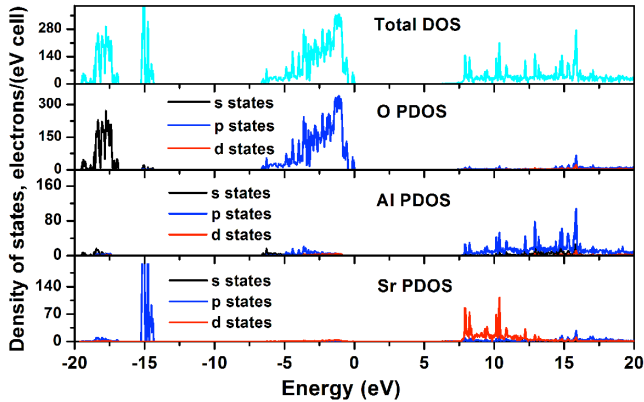
Figure 5. Total density and partial density of states of $Sr_4Al_{14}O_{25}$

The total and partial density of states (DOS) of $Sr_4Al_{14}O_{25}$ are displayed in **Figure 5**, which can offer detailed information to further understand the composition of the energy bands calculated in **Figure 4**. The two inner core bands at about -18 and -15 eV are mainly derived from the O-2s and Sr-4p states, respectively. Their narrow band character reveals a high degree of localization of those electronic states. The valence band dominated by the O-2p states stretches from -6.77 to 0 eV. The further state composition analysis on the valence band indicates the O-2p states are slight hybridized with the Al-3s, 3p states. The conduction band from 6.11 to about 15 eV is basically composed of Sr-4d states with the mixture of the Al-3p states.
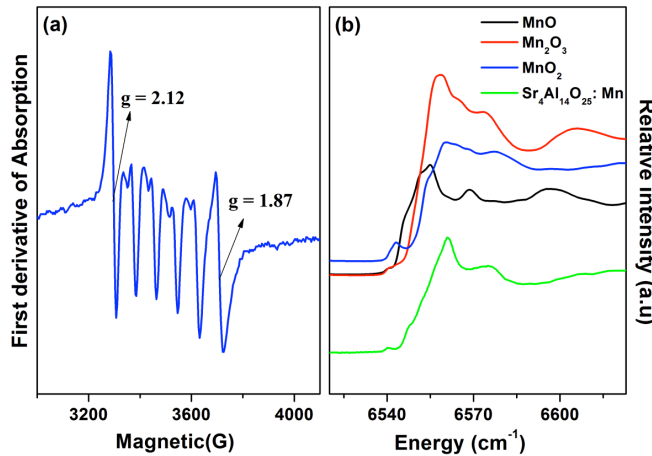
Figure 6. (a) Electron paramagnetic resonance (EPR) spectra of $Sr_4Al_{14}O_{25}$:Mn at room temperature. (b) *k*-edge XANES spectrum of $Sr_4Al_{14}O_{25}$:Mn.

Figure 6a shows the EPR spectra of $Sr_4Al_{14}O_{25}$:Mn at room temperature. The mechanism of EPR spectra of Mn ions is due to the relative magnitude between microwave frequency and crystal field splitting strength. A strong crystal field possessing the ability to make the free ion level split into five doubly degeneracy energy levels, and the remaining degeneracy is removed by the Zeeman field. In EPR spectra, additional lines of g > 2.0 and g = 2.0

are observed, which are attributed to the transitions of the unpaired electrons among the above five split levels. If the Zeeman microwave frequency is of the same order as the crystal field strength, then the zero-field resonance line appears. One good means to determine the EPR spectra of Mn ions depends on the relation between Zeeman interaction and the crystal field strength. If the value of microwave frequency is smaller than that of crystal field splitting, then the EPR signals appear only between Kramers-conjugate states, and the resonance signals can be observed at g > 2.0. On the contrary, if the value of the microwave frequency is larger than that of the crystal field splitting, then the EPR signals can be observed closed to g = 2.0. The EPR signals obtained in this work and the value of the g factor can be calculated by the following equation:

$$hv = g\beta H \tag{1}$$

Where h is the Planck constant (6.62662×10^{-27} erg/s), v is the microwave frequency, β is the Bohr magneton (9.27410×10^{-21} erg/G), and g is the nondimensional spectral splitting factor (g value). When the value of microwave frequency is 9.8 GHz, according to Eq. (1), the calculated experimental value of g is at g = 2.12 and g = 1.87 for the H = 3295 G and H = 3707 G, respectively. The results indicate that the crystal field split energy is of similar magnitude or larger than the 9.8 GHz quantum.

To determine the charge varieties of Mn, the XANES spectrum of $Sr_4Al_{14}O_{25}$:Mn were displayed in **Figure 6b**. The materials MnO, Mn_2O_3, and MnO_2 were used as references for the Mn valence states: Mn^{2+}, Mn^{3+}, and Mn^{4+}, respectively. The Mn *k*-edge XANES spectra of $Sr_4Al_{14}O_{25}$:Mn presented two peaks at 6539 cm^{-1} and 6547 cm^{-1} for Mn^{2+}, one peak at 6561 cm^{-1} for Mn^{4+} and 6570 cm^{-1} for Mn^{3+}. The results indicate that Mn^{2+}, Mn^{3+}, and Mn^{4+} coexist in $Sr_4Al_{14}O_{25}$:Mn.
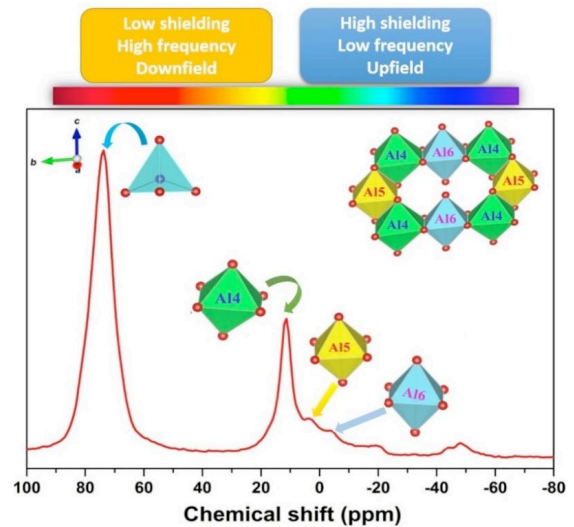
Figure 7. ^{27}Al solid-state NMR result of $Sr_4Al_{14}O_{25}$:Mn. The AlO_6 octahedral with green, yellow, and cyan colors are Al4, Al5, and Al6 sites, respectively.

The effect of crystal field environment between the activator and host can be researched by the solid-state NMR. The ^{27}Al MAS NMR spectra of $Sr_4Al_{14}O_{25}$:Mn at the 14.1 T

(20 kHz spinning rate) magnetic field is displayed in **Figure 7**. The NMR spectra shows a series of resonance peaks from -10 to 90 ppm, including one strong overlapping resonance of Al^{3+} in the frequency range from 90 to 60 ppm as well as one narrow and two broader resonances ranging from 20 to -10 ppm. In the unit cell of $Sr_4Al_{14}O_{25}$, six types of Al^{3+} site and nine types of O^{2-} site exist, and the structure of $Sr_4Al_{14}O_{25}$ consists of one layer of AlO_6 octahedra and double layers of tetrahedral AlO_4 (**Figure 1b**). Before the discussion of the relationship between the solid-state NMR chemical shift (^{27}Al) and local chemical environments in AlO_4 and AlO_6 as well as the distribution of the resonance peaks in different Al^{3+} sites, the coordination of Al^{3+} and the bond length of Al-O data are listed in **Table 2**. The data are covert to the relation, which is used to calculate the active bond valence of each Al^{3+} site based on bond valence theory and can be described as follows: [43,44]

$$S_{ij} = \exp(\frac{d_0 - d_{ij}}{C}) \tag{2}$$

The effective valence can be evaluated obeying the following formula:

$$V_i = \sum_j V_{ij} \tag{3}$$

Where d_{ij} is the length of the bond between atoms of i and j, C is a universal constant, d_0 is the parameter of Al-O bonds, and j is the coordination number (or bond number). For Al-O bond, d_0 = 1.651, C = 0.37 Å.[43,44] Thus, according to Eqs. (2) and (3), the values of bond valence are shown in **Table 2**. The active valences of Al^{3+} ions (Al1, Al2, and Al3) are close to +3, indicating that the AlO_4 tetrahedron possess strong covalence. By contrast, the active valences of Al^{3+} ions in the AlO_6 octahedron deviate from the ideal +3, which are 0.33452 lower, 0.26277 higher, and 0.13309 lower than +3 for Al4, for Al5, and for Al6, respectively, and these results are similar to those of the previous report.[45] The AlO_6 octahedron is polarized, and the polarization of Al4 site is the strongest, followed by Al5 site and then Al6 site. This order is relevant to the distribution of the resonance peaks of the NMR spectra in **Figure 7**.
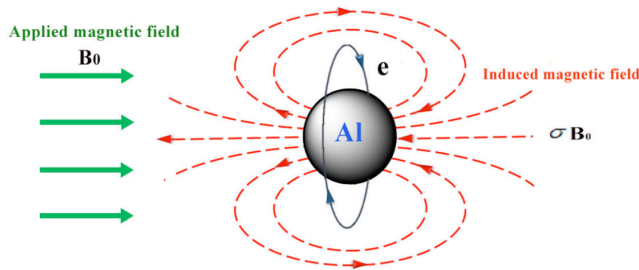
**Figure 8.** Schematic of the shielding effect of AlO_6 and AlO_4 in $Sr_4Al_{14}O_{25}$.

The resonance peaks obtained in the NMR spectra are influenced by the molecular environment and applied magnetic field.[46] The nuclear of Al^{3+} in both AlO_4 and AlO_6 structures spin at a determined magnetic field Bo, generating an induced electromagnetic field which is in opposite direction with Bo, resulting in a weakness of the

applied magnetic field (**Figure 8**), which is defined as shielding effect. The strength of induced electromagnetic field increases as the electronegativity weakens, and vice versa. The relation between applied magnetic field (magnetic field effect) and induced electromagnetic field (shielding effect) can be described in the following formula: [46]

$$B_{eff} = B_0(1-\sigma) \tag{4}$$

Where B_{eff} is the true magnetic field act on the nuclear, Bo is the applied magnetic field, and σ is the shielding factor. Compared with the AlO_6 octahedra, the AlO_4 tetrahedron show stronger covalence and electronegativity than those of the AlO_6 octahedra. According to Eq. (4), the AlO_4 tetrahedron show weaker shielding effect, stronger magnetic field effect, and bigger nuclear spin state separation energy than those of the AlO_6 octahedra. The resonance peak in low shielding, high frequency, and downfield ranging from 60 to 90 ppm is attributed to the AlO_4 tetrahedron. By contrast, the three resonance peaks in relative high shielding, low frequency, and upfield ranging from 20 to -10 ppm are assigned to the AlO_6 octahedra, which corresponds to the previous report.[45, 47] Considering the strength of the polarization of the AlO_6 octahedra in Al4, Al5, and Al6 site, the weaker the AlO_6 octahedra is polarized, the weaker the electronegativity, then the stronger shielding effect, weaker magnetic field effect, and smaller nuclear spin state separation energy. Thus, the resonance peaks ranging from 20 to 5 ppm, 5 to 0 ppm, and 0 to -10 ppm are attributed to the AlO_6 octahedral resonances in Al4, Al5, and Al6 site, respectively, which are shown in **Figure 9**, corresponding to the results previously reported.[45] In addition, the two overlapping resonances appear within the range from -40 to -55 ppm, which may be caused by the substitution of Mn ions for Al ions in octahedral sites. When Mn ions replaced Al ions, the Al5 site of the AlO_6 octahedron was compressed, whereas the Al6 site of the AlO_6 octahedron was elongated,[48] leading to change and deformation of plane (a b), and thus resulting in the appearance of the two overlapping resonances.
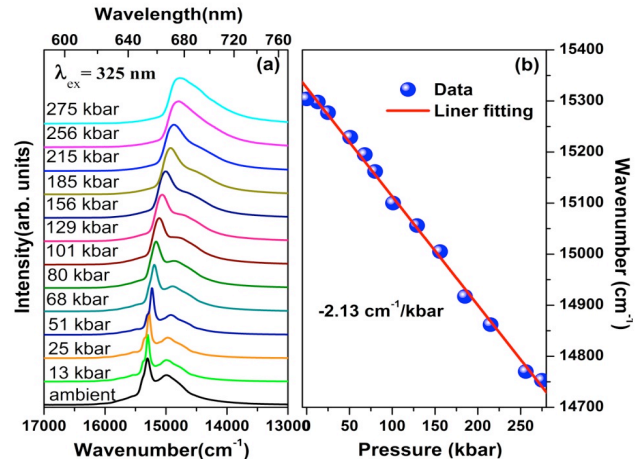
Figure 9. (a) Luminescence spectra of $Sr_4Al_{14}O_{25}$:Mn^{4+} at different pressures excited at 325 nm. (b) Position of the

dominant luminescence peak of $Sr_4Al_{14}O_{25}:Mn^{4+}$ versus pressure.

PL spectra under different pressures are demonstrated in **Figure 9a**. Both features, the R-line and the phonon repetition sideband, shift with pressure toward the lower energies. In **Figure 9b**, the energy of the R-line luminescence versus pressure is presented. The energy decreases linearly by increasing the pressure with the rate equal to -2.13 cm^{-1}/ kbar. The red shift of the R-lines is related to the nephelauxetic effect, associated to the change of repulsion of the d-electrons because of the increased covalency of the Mn^{4+}-O^{2-} bonds with the increased pressure. Such pressure behavior of the luminescence related to $^2E_g \rightarrow$ $^4A_{2g}$ transition is well known and has been reported many times for Mn^{4+}.[49-52] In the framework of the crystal-field theory,[19] the nephelauxetic effect in the spectroscopy of the Mn^{4+} ion can be understood with the help of the newly proposed parameter $\beta_1 = \sqrt{(B/B_0)^2 + (C/C_0)^2}$ by Brik et al., where B, C (B_0, C_0) are the Racah parameters of the Mn^{4+} ions in a crystal (free state), respectively. And the ^2E_g emission energy can be expressed as a linear dependence on the nephelauxetic ratio β_1 as follows: $E(^2E_g) = 16261.92\beta_1$-880.49 cm^{-1}. It can be easily derived that the nephelauxetic ratio β_1 also linearly decreases with the increasing pressure and its dimensionless variation slope is 1.3098×10^{-4}. The fact suggests the hybridization effect between the Mn-3d(t_{2g}) and O-2p states is not dramatically changed in the studied pressure range as confirmed by the smaller energy variation with about 600 cm^{-1} of the ^2E_g level position. In addition, for pressure above 100 kbar, the R-line and their sideband also become broader and strongly overlap. This effect can be explained by the inhomogeneous broadening of the emission lines related to uniaxial and tension stresses, which can accompany the high hydrostatic pressure experiments.

Table 2. Coordination of Al^{3+}, bond length, and bond valence and bond valence of Al-O of $Sr_4Al_{14}O_{25}$:Mn determined by Rietveld refinement of XRD data.

Ion	Coordination	Bond-length	Bond-valence	Active valence
Al 1	O3	1.73046 (8)	0.80037	2.92168
	O2	1.75194(5)	0.76124	
	O7	1.77360(8)	0.71795	
	O4	1.81859(7)	0.63575	
Al 2	O8	1.71726(8)	0.83604	
	O2	1.74465(8)	0.77638	3.00826
	O6	1.77840(6)	0.70870	
	O1	1.78983(6)	0.68714	
Al 3	O9	1.71090(8)	0.85053	
	O3	1.73339(6)	0.80037	3.17209
	O3	1.73339(6)	0.80037	
	O4	1.77213(8)	0.720811	
	O1	1.91952(7)	0.48397	
	O1	1.91952(7)	0.48397	
Al 4	O8	1.95834(6)	0.43577	2.66548
	O8	1.95834(6)	0.43577	
	O5	1.97819(6)	0.41300	
	O5	1.97819(6)	0.41300	
Al 5	O5	1.85102(7)	0.41300	
	O5	1.85102(7)	0.41300	
	O1	1.88977(6)	0.48397	
	O1	1.88977(6)	0.48397	3.26277
	O1	1.88977(6)	0.48397	
	O1	1.88977(6)	0.48397	
Al 6	O8	1.88559(6)	0.53045	
	O8	1.88559(6)	0.53045	
	O8	1.88559(6)	0.53045	2.86691
	O8	1.88559(6)	0.53045	
	O6	2.01633(7)	0.37255	
	O6	2.01633(7)	0.37255	
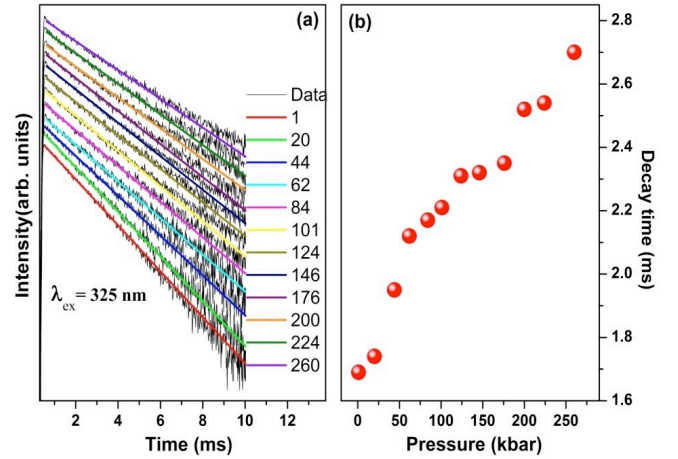
Figure 10. (a) Experimental decay curves and fitted decay curves of $Sr_4Al_{14}O_{25}:Mn^{4+}$ under different pressures observed at maximum of the $^2E_g \rightarrow$ $^4A_{2g}$ Mn luminescence excited at 325 nm. (b) Luminescence decay times under different pressures.

Time-resolved spectroscopy showed both two features, the R-line and sideband, decay exponentially with the same lifetime. The luminescence decay time becomes slower as pressure increases. This effect is clearly seen in **Figure 10a**, where the luminescence decay profiles for different pressures are presented. In **Figure 10b**, the luminescence lifetime versus pressure is presented. Luminescence lifetime increases with pressure from 1.35 ms for ambient pressure to 2.7 ms for 260 kbar.
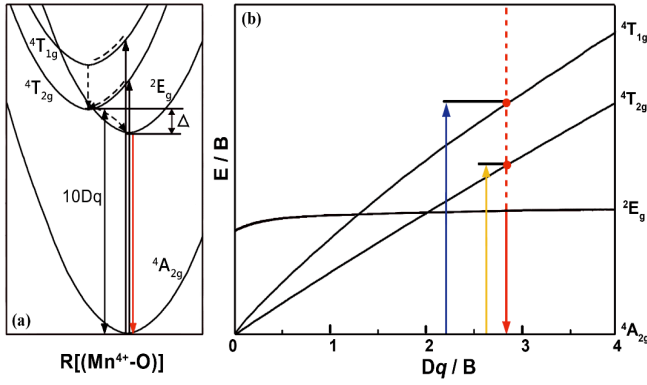
Figure 11. (a) Configurational coordinate diagram representing the $Sr_4Al_{14}O_{25}$:Mn^{4+} energetic structure. The back solid arrows represent the absorption transitions responsible for the excitation bands in **Figure 3**. The red arrow represents the luminescence transition. The dashed arrows represent non-radiative excitation processes. (b) Tanabe-Sugano diagram of $Sr_4Al_{14}O_{25}$:Mn^{4+}.

To describe pressure dependence of the R-line emission lifetime, the energetic structure of the Mn^{4+} ($3d^3$ system) should be considered. The fivefold degenerated 3d state can split into the higher e_g doubly degenerated and the lower t_{2g} triply degenerated state in the octahedral coordination. $^4A_{2g}$ state is the ground state of the Mn^{4+}, in which all three electrons occupy the lower electronic manifold t_{2g} with parallel spins. The Mn^{4+} ions can be excited through two ways; one is by exciting one electron to the e_g electronic manifold without changing its spin, leading to the excited state $^4T_{2g}$, and the other one by inversing one electron's spin without changing its electronic manifold. The latter is similar to exciting the system to the ^2E_g excited state. $^4T_{1g}$ is another next excited state, which is attributed to the t_{2g} electronic configuration. Based on the result, the absorption spectra of the Mn^{4+} ions in octahedral coordination are made up of two bands associated with spin-allowed $^4A_{2g}{\rightarrow}^4T_{2g}$ and $^4A_{2g}{\rightarrow}^4T_{1g}$ transitions. The energetic structure of the Mn^{4+} in $Sr_4Al_{14}O_{25}$ is presented by configurational coordinate diagram in **Figure 11a**, where these transitions are displayed by solid black arrows.

The values of the electronic-state energies of Mn^{4+} ions center are based on the values of Racah parameters B and C, which describes the Coulomb repulsion interaction between the 3d electrons and the crystal field strength 10Dq. The 10Dq describes the interaction between the 3d electrons and their ligands (the nearest oxygen ions) which form an approximately ideal octahedron with the Mn^{4+} ion as the center. The value of 10Dq is equal to the e_g-t_{2g} splitting and is proportional to the Mn^{4+}-O^{2-} interionic distance R as R^{-t} (t depends on host and is usually greater than 5).[53] The results show that the energy of the $^4T_{2g}$ state with regard to the ground state is equal to the crystal field strength 10Dq. On the contrary, the energy of the lowest doublet ^2E_g with regard to the ground state is almost constant and weakly dependent on the crystal field, but correlated to the 3d Coulomb interaction. Dependence of the energetic structure of the Mn^{4+} on the

value of Dq can be presented by the Tanabe–Sugano diagram (**Figure 11b**).

The $^2E_g{\rightarrow}^4A_{2g}$ transition is spin forbidden; therefore, the R luminescence lifetime τ_E is in ms range and depends on the spin-orbit coupling that mixes the ^2E_g and $^4T_{2g}$ states, described by Hamiltonian H_{s-0}. Several sophisticated models [50, 54] allow the calculation of the dependence of the R-line luminescence lifetime on the $^4T_{2g}$ and ^2E_g separation energy Δ, spin-orbit coupling, and radiative lifetime of the $^4T_{2g}$ state τ_T. However, for the interpretation of the data presented in **Figures 10a** and **b**, we use the simplified relation, which is given as follows:

$$\frac{1}{\tau_E} = \frac{1}{\tau_T}\frac{H_{s-0}^2}{\Delta^2} \tag{5}$$

Pressure compresses the lattice and diminishes the Mn^{4+}-ligand distance R. As a result, the energy of the $^4T_{2g}$ state and energy Δ increases with pressure. Seeing that pressure does not change or slightly changes the spin-orbit coupling and $^4T_{2g}$ state lifetime τ_T, it yields the increase of the R-line ($^2E_g \rightarrow {}^4A_{2g}$ transition) luminescence lifetime.
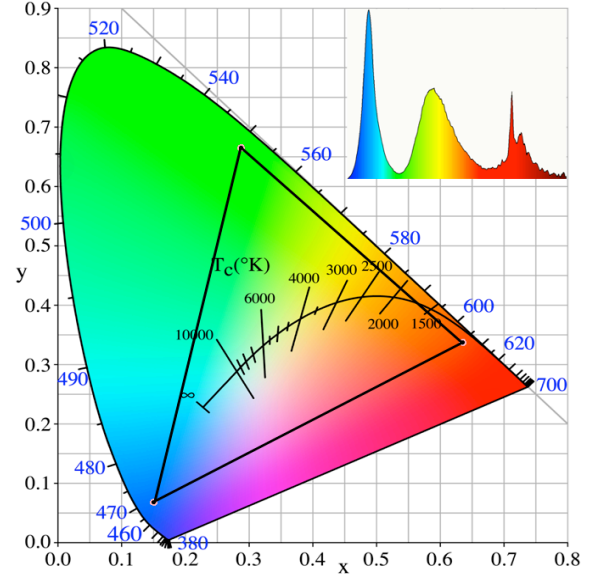
Figure 12. A typical triangle color gamut for backlighting application of tri-color display device. The inserted diagram shows tri-color display spectrum using InGaN blue chip, **β**-SiAlON:Eu^{2+} green phosphor, and $Sr_4Al_{14}O_{25}$:Mn.

The tri-color display spectrum by combining blue InGaN chips, commercial **β**-SiAlON:Eu^{2+} green phosphor, and $Sr_4Al_{14}O_{25}$:Mn red phosphor were evaluated for commercial applications. The full spectrum and high color purity with narrow band green and red phosphors are shown in the inset of **Figure 12**. The color gamut of display lighting is determined by coordinates in Commission Internationale de l'Éclairage diagram. The figure illustrates the possibility of color gamut in the triangle region. It is accessible for fabricating devices by making the WLED with the present red phosphor as phosphor-converted LED backlighting source.

■ CONCLUSIONS

The Mn-doped $Sr_4Al_{14}O_{25}$ phosphors show bright red emission under n–UV excitation. DFT calculations were used to analyze the electronic structure of the $Sr_4Al_{14}O_{25}$ host, indicating that $Sr_4Al_{14}O_{25}$ is an indirect semiconductor with a band gap of approximately 6.11 eV. And thus all the bands in the PLE spectrum should be due to the introduction of the dopant Mn^{4+} ions. In addition, the crystal field split energy of Mn ions is of similar magnitude to or larger than the 9.8 GHz quantum. The effect of crystal field environment between the activator Mn and $Sr_4Al_{14}O_{25}$ host was researched. PL spectra at different pressures indicate that the R-line and the sideband shift linearly with pressure toward the lower energies because of the nephelauxetic effect. The luminescence lifetime increases from 1.35 ms for ambient pressure to 2.7 ms for 260 kbar, which is attributed to diminish the effect of the lowest quartet state $^4T_{2g}$ to the first excited state ^2E_g as pressure increases. A phosphor-converted LED device as backlighting source was developed by adding $Sr_4Si_{14}O_{25}$:Mn red phosphor into the system blue InGaN chips and commercial β-SiAlON:Eu^{2+} green phosphor. We aimed at improving the performance of the color gamut and luminous efficiency of the $Sr_4Al_{14}O_{25}$:Mn-based WLED in the future by optimizing the morphology and revising the composition.

■ ASSOCIATED CONTENT

Supporting Information

EDS result recorded from a piece of fragment (Figure S1); HRTEM image of the $Sr_4Si_{14}O_{25}$:Mn^{4+} (Figure S2); calculated and experimental structural data for neat $Sr_4Al_{14}O_{25}$ (Table S1); experimental data of $Sr_4Al_{14}O_{25}$:Mn^{4+} determined by EDS (Table S2). This material is available free of charge via the Internet at http://pubs.acs.org.

■ AUTHOR INFORMATION

Corresponding Authors

* E-mail: cgma.ustc@gmail.com (C. G. Ma) Tel: +86 136 4765 9358

* E-mail: guocf@nwu.edu.cn (C. F. Guo) Tel: +86 29 8830 2661

* E-mail: rsliu@ntu.edu.tw (R. S. Liu) Tel: +886 2 3366 1169

Author Contributions

All authors have given approval to the final version of the manuscript.

Notes

The authors declare no competing financial interest.

■ ABBREVIATIONS

SEM, scanning electron microscopy; XRD, X-ray diffraction; TPAS, Total Pattern Analysis Solutions; PL, photoluminescence; PLE, photoluminescence excitation; DFT, density functional theory; GGA, generalized gradient approximation; HRTEM, high-resolution transmission electron microscope; NMR, nuclear magnetic resonance; ESR, electron spin resonance.

■ REFERENCES

(1) Lin, C. C.; Xiao, Z. R.; Guo, G. Y.; Chan, T. S.; Liu, R. S. Versatile Phosphate Phosphors $ABPO_4$ in White Light-Emitting Diodes: Collocated Characteristic Analysis and Theoretical Calculations. *J. Am. Chem. Soc.* **2010**, *132*, 3020-3028.

(2) Wang, B.; Lin, H.; Xu, J.; Chen, H.; Wang, Y. S. $CaMg_2Al_{16}O_{27}$:Mn^{4+}-Based Red Phosphor: A Potential Color Converter for High-Powered Warm W‑LED. *ACS Appl. Mater. Interfaces* **2014**, *6*, 22905-22913.

(3) Shang, M. M.; Li, C. X.; Lin, J. How to Produce White Light in A Single-Phase Host? *J. Chem. Soc. Rev.* **2014**, *43*, 1372-1386.

(4) Lin, H.; Wang, B.; Xu, J.; Zhang, R.; Chen, H.; Yu, Y. L.; Wang, Y. S. Phosphor-in-Glass for High-Powered Remote-Type White AC-LED. *ACS Appl. Mater. Interfaces* **2014**, *6*, 21264-21269.

(5) Chen, Y. B.; Gong, M. L.; Wang, G.; Su, Q. High Efficient and Low Color-Temperature White Light-emitting Diodes with $Tb_3Al_5O_{12}$: Ce^{3+} Phosphor. *Appl. Phys. Lett.* **2007**, *91*, 071117-071119.

(6) Tsai, Y. T.; Chiang, C. Y.; Zhou, W. Z.; Lee, J. F.; Sheu, H. S.; Liu, R. S. Structural Ordering and Charge Variation Induced by Cation Substitution in (Sr, Ca)$AlSiN_3$:Eu Phosphor. *J. Am. Chem. Soc.* **2015**, *137*, 8936-8939.

(7) Chen, W. T.; Sheu, H. S.; Liu, R. S.; Attfield, J. P. Cation-Size-Mismatch Tuning of Photoluminescence in Oxynitride Phosphors. *J. Am. Chem. Soc.* **2012**, *134*, 8022-8025.

(8) Xie, R. J.; Hirosaki, N.; Suehiro, T.; Xu, F. F.; Mitomo, M. A Simple, Efficient Synthetic Route to $Sr_2Si_5N_8$:Eu^{2+}-Based Red Phosphors for White Light-Emitting Diodes. *Chem. Mater.* **2006**, *18*, 5578-5583.

(9) Pust, P.; Wochnik, A. S.; Baumann, E.; Schmidt, P. J.; Wiechert, D.; Scheu, C.; Schnick, W. $Ca[LiAl_3N_4]$:Eu^{2+}-A Narrow-Band Red-Emitting Nitridolithoaluminate. *Chem. Mater.* **2014**, *26*, 3544-3549.

(10) Yeh, C. W.; Chen, W. T.; Liu, R. S.; Hu, S. F.; Sheu, H. S.; Chen, J. M.; Hintzen, H. T. Origin of Thermal Degradation of $Sr_{2-x}Si_5N_8$:Eu_x Phosphors in Air for Light-Emitting Diodes. *J. Am. Chem. Soc.* **2012**, *134*, 14108-14117.

(11) Lv, W. Z.; Jiao, M. M.; Zhao, Q.; Shao, B. Q.; Lv, W.; You, H. P. $Ba_{1.3}Ca_{0.7}SiO_4$:Eu^{2+}, Mn^{2+}: A Promising Single-Phase, Color-Tunable Phosphor for Near-Ultraviolet White-Light-Emitting Diodes. *Inorg. Chem.* **2014**, *53*, 11007-11014.

(12) Guo, C. F.; Chu, B. L.; Wu, M. M.; Su, Q. Oxide Coating for Alkaline Earth Sulfide Based Phosphor. *J. Lumin.* **2003**, *105*, 121-126.

(13) Peng, M. Y.; Yin, X. W.; Tanner, P. A.; Liang, C. Q.; Li, P. F.; Zhang, Q. Y.; Qiu, J. R. Orderly-Layered Tetravalent Manganese-Doped Strontium Aluminate $Sr_4Al_{14}O_{25}$:Mn^{4+}: An Efficient Red Phosphor for Warm White Light Emitting Diodes. *J. Am. Ceram. Soc.* **2013**, *96*, 2870-2876.

(14) Peng, M. Y.; Yin, X. W.; Tanner, Peter A.; Brik, M. G.; Li, P. F. Site Occupancy Preference, Enhancement Mechanism, and Thermal Resistance of Mn^{4+} Red Luminescence in $Sr_4Al_{14}O_{25}$:Mn^{4+} for Warm WLEDs. *Chem. Mater.* **2015**, *27*, 2938-2945.

(15) Chen, L.; Zhang, Y.; Liu, F. Y.; Zhang, W. H.; Deng, X. R.; Xue, S. C.; Luo A. Q.; Jiang, Y.; Chen, S. F. The Red Luminescence of $Sr_4Al_{14}O_{25}$: Mn^{4+} Enhanced by Coupling with the $SrAl_2O_4$ Phase in the $3SrO·5Al_2O_3$ System. *Phys. Status Solidi A* **2013**, *210*, 1791-1796.

(16) Xu, Y. D.; Wang, D.; Wang, L.; Ding, N.; Shi, M.; Zhong, J. G.; S. Qi. Preparation and Luminescent Properties of a New Red Phosphor ($Sr_4Al_{14}O_{25}$:Mn^{4+}) for White LEDs. *J. Alloys Compd.* **2013**, *550*, 226–230.

(17) Meng, L. L.; Liang, L. F.; Wen, Y. X. A Novel Red Phosphor Na^+, Mn^{4+} Co-Doped $Sr_4Al_{14}O_{25}$ for Warm White Light Emitting Diodes. *Mater. Chem. Phys.* **2015**, *153*, 1-4.

(18) Grinberg, M.; Suchoki, A. Pressure-Induced Changes in the Energetic Structure of the $3d^3$ Ions in Solid Matrices. *J. Lumin.* **2007**, *125*, 97-103.

(19) Brik, M. G.; Camardello, S. J.; Srivastava, A. M. Influence of Covalency on the Mn^{4+} $^2E_g \rightarrow ^4A_{2g}$ Emission Energy in Crystals. *ECS J. Solid State Sci. Technol.* **2015**, *4*, R39-R43.

(20) Du, M.-H. Chemical Trends of $Mn4^+$ Emission in Solids. *J. Mater. Chem. C* **2014**, *2*, 2475-2481.

(21) Dovesi, R.; Saunders, V. R.; Roetti, C.; Orlando, R.; Zicovich-Wilson, C. M.; Pascale, F.; Civalleri, B.; Doll, K.; Harrison, N. M.; Bush, I. J.; Llunell, M.; Causà, M.; Noël, Y. *CRYSTAL14 User's Manual*, University of Torino, Torino, **2014**.

(22) Demichelis, R.; Civalleri, B.; Ferrabone, M.; Dovesi, R. On the Performance of Eleven DFT Functionals in the Description of the Vibrational Properties of Aluminosilicates. *Int. J. Quantum Chem.* **2010**, *110*, 406-415.

(23) Demichelis, R.; Noël, Y.; Civalleri, B.; Roetti, C.; Ferrero, M.; Dovesi, R. The Vibrational Spectrum of α-AlOOH Diaspore: An Ab Initio Study with the CRYSTAL Code. *J. Phys. Chem. B* 2007, *111*, 9337-9346.

(24) Bredow, T.; Jug, K.; Evarestov, R. A. Electronic and Magnetic Structure of $ScMnO_3$. *Phys. Status Solidi B* **2006**, *243*, R10-R12.

(25) Kaupp, M.; Schleyer, P. V. R.; Stoll, H.; Preuss, H. Pseudopotential Approaches to Ca, Sr, and Ba Hydrides. Why Are Some Alkaline Earth MX_2 Compounds Bent? *J. Chem. Phys.* **1991**, *94*, 1360-1366.

(26) Wang, D.; Wang, M. Q.; Lv, G. L. Synthesis, Crystal Structure and X-ray Powder Diffraction Data of the Phosphor Matrix $4SrO·7Al_2O_3$. *J. Mater. Sci.* **1999**, *34*, 4959-4964.

(27) Nadezhina, T. N.; Pobedimskaya, E. A.; Belov, N. V. Coordination Polyhedra of Strontium in the Structures Sodium Strontium Germanate($Na_4SrGe_3O_3[GeO_4]_3$), Strontium Germinate($Sr_3[Ge_3O_9]$), Strontium Aluminate($Sr_4Al_4O_2[Al_{10}O_{23}]$) and Bis(hydroxystrontium) Tetrahydroxy Cuprate (II)$Sr_2(OH)_2[Cu(OH)_4]$. *Kristallografiya* **1980**, *25*, 938-943.

(28) Bergstein, A.; White, W. B. Manganese-Activated Luminescence in $SrAl_{12}O_{19}$ and $CaAl_{12}O_9$. *J. Electrochem. Soc.* **1971**, *118*, 1166-1171.

(29) Lindop, A. J.; Goodwin, D. W. The Refined Structure of $SrO·2Al_2O_3$. *Acta Crystallogr., Sect. B: Struct. Crystallogr. Cryst. Chem.* **1972**, *28*, 2625-2626.

(30) Angel, R. J.; Prewitt, C. T. Crystal Structure of Mullite: A Re-Examination of the Average Structure. *Am. Mineral.* **1986**, *71*, 1476-1482.

(31) Su, Z. X.; Dickinson, C. Wan, Y. T.; Wang, Z. L.; Wang, Y. W.; Sha, J.; Zhou, W. Z. Crystal Growth of Si Nanowires and Formation of Longitudinal Planar Defects. *CrystEngComm.* **2010**, *12*, 2793-2798.

(32) Jin, Y.; Fang, M. H.; Grinberg, M.; Mahlik, S.; Lesniewski, T.; Brik, M. G. ; Luo, G. Y.; Lin, J. G.; Liu, R. S. Narrow Red Emission Band Fluoride Phosphor $KNaSiF_6$:Mn^{4+} for Warm White Light-Emitting Diodes. ACS Appl. Mater. Interfaces **2016**, 8, 11194-11203.

(33) Sherman, D. M. The Electronic Structures of Manganese Oxide Minerals. *Am. Mineral.* **1984**, *69*, 788-799.

(34) Wang, B.; Lin, H.; Huang, F.; Xu, J.; Chen, H.; Lin, Z. B.; Wang. Y. S. Non-Rare-Earth $BaMgAl_{10-2x}O_{17}$:xMn^{4+}, xMg^{2+}: A Narrow-Band Red Phosphor for Use as a High-Power Warm w-LED. *Chem. Mater.* **2016**, *28*, 3515-3524.

(35) Chen, H.; Lin, H.; Huang, Q. M.; Huang, F.; Xu, J.; Wang, B.; Lin, Z. B.; Zhou, J. C.; Wang, Y. S. A Novel Double-Perovskite Gd_2ZnTiO_6:Mn^{4+} Red Phosphor for UV-Based w-LEDs: Structure and Luminescence Properties. *J. Mater. Chem. C* **2016**, *4*, 2374-2381.

(36) Zhu, H. M.; Lin, C. C.; Luo, W. Q.; Shu, S.; Liu, Z. G.; Liu, Y. S.; Kong, J. T.; Ma, E.; Cao, Y. G.; Liu, R. S.; Chen, X. Y. Highly Efficient Non-Rare-Earth Red Emitting Phosphor for Warm White Light-Emitting Diodes. *Nat. Commun.* **2014**, *4312*, 1-10.

(37) Srivastava, A. M.; Beers, W. W. Luminescence of Mn^{4+} in the Distorted Perovskite Gd_2MgTIO_6. *J. Electrochem. Soc.* **1996**, *143*, L203-L205.

(38) Murata, T.; Tanoue, T.; Iwasaki, M.; Morinaga, K.; Hase, T. Fluorescence Properties of Mn^{4+} in $CaAl_{12}O_{19}$ Compounds as Red-Emitting Phosphor for White LED. *J. Lumin.* **2005**, *114*, 207-212.

(39) Setlur, A. A.; Radkov, E. V.; Henderson, C. S.; Her, J. H.; Srivastava, M. A.; Karkada, N.; Kishore, M. S.; Kumar, N. P.; Aesram, D.; Deshpande, A.; Kolodin, B.; Grigorov, L. S.; Happek, U. Energy-Efficient, High-Color-Rendering LED Lamps Using Oxyfluoride and Fluoride Phosphors. *Chem. Mater.* **2010**, *22*, 4076-4082.

(40) Matsuzawa, T.; Aoki, Y.; Takeuchi, N.; Murayama, Y. A New Long Phosphorescent Phosphor with High Brightness, $SrAl_2O_4$:Eu^{2+}, Dy^{3+}. *J. Electrochem. Soc.* **1996**, *143*, 2670-2673.

(41) Obukuro, Y.; Matsushima, S.; Nakamura, H.; Arai, M.; Yamada, H.; Xu, C.-N. Electronic Structure of Eu^{2+}-Doped $SrAl2O4$ Using Modified Becke-Johnson Exchange Potential. *Solid State Commun.* **2014**, *186*, 46-49.

(42) Nazarov, M.; Brik, M. G.; Spassky, D.; Tsukerblat, B.; Nazida, A. N.; Ahmad-Fauzi, M. N. Structural and Electronic Properties of $SrAl_2O_4$:Eu^{2+} from Density Functional Theory Calculations. *J. Alloys Compd.* **2013**, *573*, 6-10.

(43) Santoro, A.; Sora, I. N.; Huang, Q. Bond-Valence Analysis of the Structure of $(Ba_{0.875}Sr_{0.125})RuO_3$. *J. Solid State Chem.* **1999**, *143*, 69-73.

(44) Song, Z.; Liao, J.; Ding, X. L.; Zhou, T. L.; Liu, Q. L. Stability of Divalent/Trivalent Oxidation State of Europium in Some Sr-Based Inorganic Compounds. *J. Lumin.* **2012**, *132*, 1768-1773.

(45) Chen, L.; Xue, S. C.; Chen, X. L.; Bahader, A. Deng, X. R.; Zhao, B. L.; Jiang, Y.; Chen, S. F.; Chan, T. S.; Zhao, Z.; Zhang, W. H. The Site Occupation and Valence of Mn Ions in the Crystal Lattice of $Sr_4Al_{14}O_{25}$ and Its Deep Red Emission for High Color-Rendering White Light-Emitting Diodes. *Mater. Res. Bull.* **2014**, *60*, 604-611.

(46) Fitzgerald, J. J.; DePaul, S. M. *Solid-State NMR Spectroscopy of Inorganic Materials: An Overview,* ACS Symposium Series; American Chemical Society: Washington, DC, 1999; 717, Chapter 1, pp 2-133.

(47) Capron, M.; Fayon, F.; Massiot, D.; Douy, A. $Sr_4Al_{14}O_{25}$: Formation, Stability, and ^{27}Al High-Resolution NMR Characterization. *Chem. Mater.* **2003**, *15*, 575-579.

(48) Jia, Y. C.; Qiao, H.; Guo, N.; Zheng, Y. H.; Yang, M.; Huang, Y. J.; You, H. P. Electronic Structure and Photoluminescence Properties of Eu^{2+}-Activated $Ca_4Si_2O_7F_2$. *Opt. Mater.* **2011**, *33*, 1803-1807.

(49) Jovanić, B. R. Shift Under Pressure of the Luminescence Transitions of Oorundum Doped with Mn^{4+}. *J. Lumin.* **1997**, *75*, 171-174.

(50) Galanciak, D.; Grinberg, M.; Gryk, W.; Kobyakov, S.; Suchocki, A.; Boulon, G.; Brenier, A. Influence of High Pressure on

the Luminescence Transitions of Mn^{4+}-Doped Gadolinium Gallium Garnet. *J. Phys.: Condens. Matter* **2005**, *17*, 7185-7197.

(51) Brenier, A.; Suchocki, A.; Pedrini, C.; Boulon, G.; Madej, C. Spectroscopy of Mn^{4+}-Doped Ca-Substituted Gadolinium Gallium Garnet. *Phys. Rev. B* **1992**, *46*, 3219-3227.

(52) Zhydachevskii, Y.; Galanciak, D.; Kobyakov, S.; Berkowski, M.; Kamińska, A.; Suchocki, A.; Zakharko, Y.; Durygin, A. Photo-Luminescence Studies of Mn^{4+} Ions in $YAlO_3$ Crystals at Ambient and High Pressure. *J. Phys.: Condens. Matter.* **2006**, *18*, 11385-11396.

(53) Chen, J. Y.; Zhang, N. M.; Guo, C. F.; Pan, F, J.; Zhou, X. J.; Suo, H.; Zhao, X. Q.; Goldys, E. M. Site-Dependent Luminescence and Thermal Stability of Eu^{2+} Doped Fluorophosphate toward White LEDs for Plant Growth. *ACS Appl. Mater. Interfaces* **2016**, *8*, 20856-20864.

(54) Grinberg, M. $^2E \rightarrow {}^4A_2$ Fluorescence of Cr^{3+} in High and Intermediate Field Garnets. *J. Lumin.* **1993**, *54*, 369-382.

TOC Graphic